Solar Physics (2005) 230: 141–167

THE SPECTRAL IRRADIANCE MONITOR: SCIENTIFIC REQUIREMENTS, INSTRUMENT DESIGN, AND OPERATION MODES

JERALD HARDER, GEORGE LAWRENCE, JUAN FONTENLA,
GARY ROTTMAN and THOMAS WOODS
Laboratory for Atmospheric and Space Physics, University of Colorado, Boulder, U.S.A.
(e-mail: jerald.harder@lasp.colorado.edu)

(Received 20 January 2005; accepted 30 March 2005)

Abstract. The Spectral Irradiance Monitor (SIM) is a dual Fèry prism spectrometer that employs 5 detectors per spectrometer channel to cover the wavelength range from 200 to 2700 nm. This instrument is used to monitor solar spectral variability throughout this wavelength region. Two identical, mirror-image, channels are used for redundancy and in-flight measurement of prism degradation. The primary detector for this instrument is an electrical substitution radiometer (ESR) designed to measure power levels ∼1000 times smaller than other radiometers used to measure TSI. The four complementary focal plane photodiodes are used in a fast-scan mode to acquire the solar spectrum, and the ESR calibrates their radiant sensitivity. Wavelength control is achieved by using a closed loop servo system that employs a linear charge coupled device (CCD) in the focal plane. This achieves 0.67 arcsec control of the prism rotation angle; this is equivalent to a wavelength positioning error of $\delta\lambda/\lambda = 150$ parts per million (ppm). This paper will describe the scientific measurement requirements used for instrument design and implementation, instrument performance, and the in-flight instrument operation modes.

1. Introduction

This paper describes the Spectral Irradiance Monitor (SIM) on the Solar Irradiance and Climate Experiment (SORCE). SORCE was launched on 25 January 2003, and the four instruments on the satellite are designed to study spectral and total solar irradiance with very high accuracy over a broad wavelength range. SIM was developed to replace and extend the UARS SOLSTICE N-channel spectrometer (Rottman, Woods, and Sparn, 1993) that was used to study solar variability in the 280–420 nm region. The SIM instrument covers a much wider spectral range (200–2700 nm) and uses an electrical substitution radiometer (ESR) as its primary detector. A Fèry prism is used in place of a grating, allowing for full wavelength range with only one optical element, thereby simplifying the spectrometer design and operation. The preliminary design and operation of the instrument was documented in two manuscripts prior to this comprehensive study (Harder *et al.*, 2000a; Harder *et al.*, 2000b).

Starting in the mid 1980s the majority of the extra-atmospheric measurements of solar spectral irradiance have concentrated on the more variable ultraviolet spectrum (London *et al.*, 1993) because of its importance to stratospheric ozone trends and

mid-latitude stratospheric circulation (Labitzske and Van Loon, 1988; Hood, 1999). These studies show that ultraviolet variability ranges from about 10% at 200 nm to about 0.1% at 300 nm over the length of a solar cycle. In the visible and near-infrared (NIR) however, there is a paucity of spectral irradiance data and the secular trends have been estimated from measurements of the total solar irradiance (TSI) performed by satellite-borne active cavity radiometers that have an exquisitely high absolute accuracy and precision (Kopp, Lawrence, and Rottman, 2003; Willson, 1988), but cannot provide the needed wavelength dependent information about spectral variability. This wavelength information is important to both solar and Earth atmospheric physics: in solar physics it is used in the interpretation of flux variability of emerging solar surface features, such as sunspots and plage (Solanki and Unruh, 1998), and in the Earth sciences it is needed to understand the strongly wavelength dependent radiation absorption processes in the atmosphere and oceans that absorb this variable solar flux (Reid, 1999; Kiehl and Trenberth, 1997). The importance of wavelength dependent information for the Earth's atmosphere is demonstrated in Figure 1 showing a MODTRAN-generated top of the atmosphere irradiance calculation at a resolution of 1 nm (Anderson *et al.*, 1999). It then shows the penetration of this radiation to the Earth's surface under equatorial, sea level, and cloud free conditions and indicates the dominant O_2, O_3, H_2O, and CO_2 atmospheric absorptions. Finally the surface radiation is propagated into the first 10 meters of ocean water (Curcio and Petty, 1951; Smith and Baker, 1978) and suggests the importance of long wavelength radiation and its variability on ocean circulation

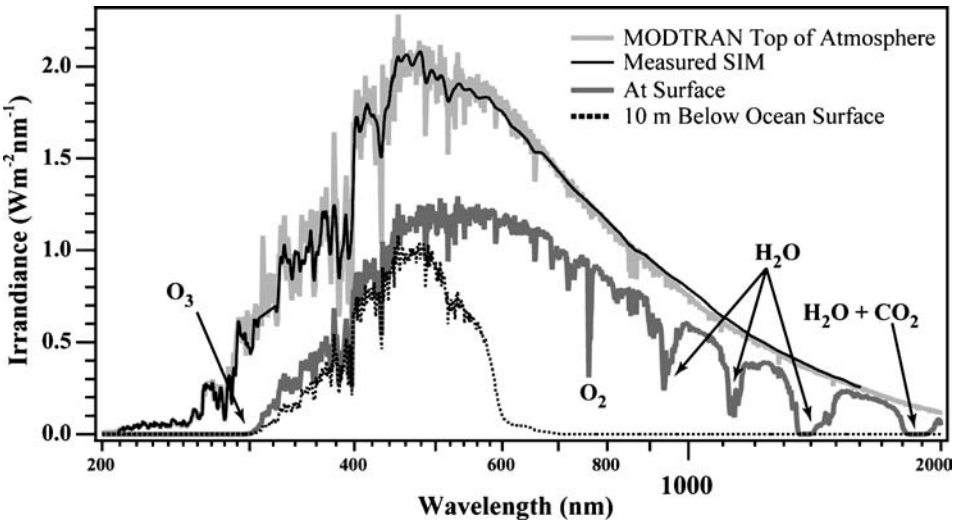

Figure 1. Penetration of the top of the atmosphere radiation into the Earth's atmosphere and oceans. The dominant molecular absorbers are noted in the graph. The graph also shows the 1 nm resolution MODTRAN top of the atmosphere solar spectrum overplotted with the measured SIM spectrum covering the wavelength range of 208 to 1604 nm.

processes (Reid, 1991; White *et al.*, 1997). Also shown in this figure is the measured SIM irradiance in the 208–1604 nm range covered by the SIM photodiode detectors discussed in Section 2.3.1.

The most frequently used modern information on the solar spectrum in the visible and NIR arises from two primary sources: the Kitt Peak solar atlas of the solar spectrum (Kurucz, 1991) in conjunction with the Neckel and Labs radiometric calibration (Neckel and Labs, 1984), and the SOLSPEC spectra (Thuillier *et al.*, 2003) acquired during the ATLAS and EURECA missions. The Kurucz spectrum is measured at a resolution of 0.055 cm^{-1} (0.0014 nm at 400 nm), so individual solar Fraunhofer lines are resolved, but do not possess an absolute calibration through the strongly scattering and absorbing Earth atmosphere. The space-based SOLSPEC spectrum, measured at a resolution of 1.0 nm in the 200–870 nm region and 20 nm in the 850–2500 nm region, has an excellent absolute laboratory calibration and does not require atmospheric corrections, but like the Labs and Neckel spectrum, cannot address solar variability because the time series is limited to only a few days during the ATLAS campaigns. Therefore, the central purpose of the SIM instrument is to measure the daily solar spectral variability in the visible and NIR and maintain an accurate absolute calibration for both solar and Earth science studies.

2. Realization of Instrument Requirements for Spectral Variability Studies

2.1. HIGH-LEVEL INSTRUMENT REQUIREMENTS

Instrument requirements for a spectral radiometer were derived from an analysis of the TSI record and theoretical estimates of variability in the visible and IR over solar cycle length records (Solanki and Unruh, 1998; Lean, 1991). The TSI record bounds the magnitude of the spectral variability: typically, solar rotation modulation is on the order of 0.2% with peak-to-peak differences of 0.1% over the course of the 11-year solar cycle. Theoretical studies on the wavelength dependence of variability produced by the emergence of active regions predict a much smaller response in the visible/IR regions with the relative variability in the 200–300 nm range from 2% to 0.5%, but less than 0.5% in the 300–1000 nm region. Thus the requirement to measure solar variability in the visible and IR spectral regions is that the instrument must have a combined precision and measurement drift stability of about 100 ppm and this condition must be valid over the 200–2000 nm region; an order of magnitude of wavelength coverage representing ∼95% of the TSI. The accuracy is based on the current standards used to measure radiant power and the needs of the atmospheric and solar physics communities; at the present time this is about 1–2%. As solar and Earth atmospheric models become more sophisticated, and as calibration standards and methods improve, accuracy will become a more stringent requirement in future studies of solar variability. The resolution required for a spectral radiometer is a function of wavelength. The resolution and spectral

sampling must be high enough in the 200 to 400 nm region to allow meaningful instrument intercomparison with currently existing instruments such as SOLSTICE, SUSIM, SOLSPEC (Rottman, Woods, and Sparn, 1993; Vanhoosier *et al.*, 1981; Thuillier *et al.*, 2003, respectively). If the resolution is too low, the spectrum becomes biased due to the rapidly changing nature of the UV spectrum, and the measurement of the important Mg II index becomes more difficult (Viereck and Puga, 1999). Therefore, in the ultraviolet the resolution must be about 1 nm. In the visible and NIR (400–2700 nm), lower spectral resolution is acceptable due to the fact that density of solar Fraunhofer lines become smaller and the effects of spectral smoothing by low resolution instruments are not as important as they are in the UV. Rottman *et al.* (2005) demonstrate that a resolution of 1–35 nm is adequate to study solar variability in this spectral region if the instrument has high enough radiometric precision. For a spectral radiometer the sources of accuracy and precision can be partitioned into three categories that must be addressed in the instrument design: (1) radiometric accuracy and precision, (2) wavelength accuracy, and (3) the maintenance of long-term instrument calibration that can be degraded by the space environment.

These needs are addressed in the SIM instrument in the following ways. (1) The radiometric accuracy scale is based on the electrical substitution principle with unit level calibrations of spectrometer components to account for light loss processes prior to the detection of radiant power. (2) The wavelength standard is based on the solar spectrum itself, and high precision of the wavelength drive is needed for spectrum-to-spectrum reproducibility without distortion. (3) SIM is designed to have two mirror-image spectrometers built into the same case that can be used for side-by-side comparisons and can be optically coupled to permit inter-instrument calibration.

2.2. Principle of design for the SIM instrument

The functionality needed to meet the requirements presented in the previous section can be represented in a block diagram form that describes three independent optical paths through the SIM instrument along with their associated electromechanical mechanisms. This block diagram is illustrated in Figure 2. Figure 3 shows two orthogonal cross-sectional views through one of the spectrometers (SIM A), and Figure 4 shows the focal plane assembly in greater detail to accompany Figure 3. The next three subsections refer to these three figures.

2.2.1. *The Spectrometer Path*

The spectrometer path provides the calibrated irradiance measurement. After passing through the front end baffle set, the light beam encounters a retractable light filter called the 'hard radiation trap' (HRT) which is a window made from Suprasil 300 (Hereaus Amersil, Inc.), the same material used to construct the prism, and acts as a light filter to absorb radiation of wavelengths less than 160 nm to reduce exposure

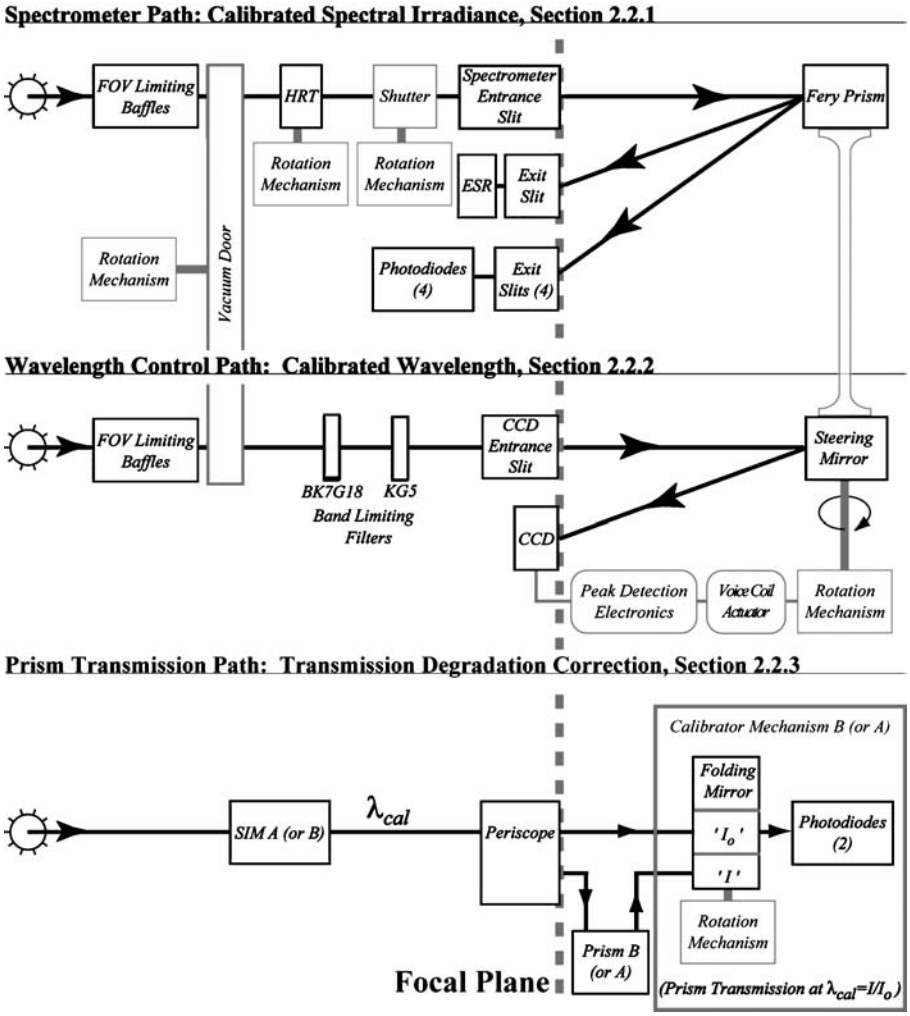

Figure 2. Block diagram of the SIM instrument. It shows three independent optical paths for irradiance measurement (spectrometer path), wavelength control, and prism transmission. The subsections in the text are labeled in the block diagram. Electrical/mechanical components are shown in gray and optical components and pathways are shown in black. Note that for the prism transmission measurement path, one of the blocks represents an entire channel of SIM.

of the prism to UV radiation known to degrade the transmission of the prism glass. The HRT is rotated out of the light path for absolute spectral measurements but is placed in the beam about 80% of the time for measurements that monitor relative solar changes. This window is tilted at 2 degrees so surface reflections will not propagate through the spectrometer, and it is wedged at 1/2° to prevent etalon effects (channeling) from distorting the spectrum. The light beam then encounters a light shutter directly in front of the spectrometer entrance slit. This shutter operates

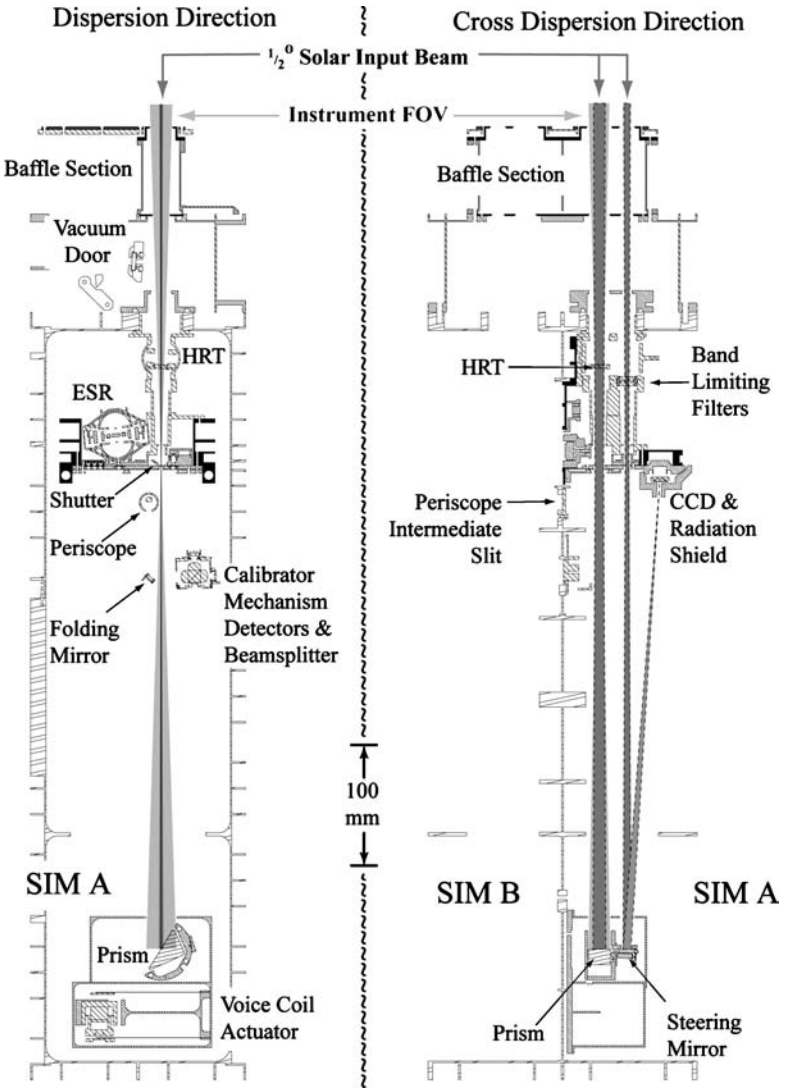

Figure 3. Two orthogonal cross-sectional views of the SIM instrument identifying critical mechanisms represented in the Figure 2 block diagram. Solar and instrument fields of view are shown as shades of gray.

synchronously with the operation of the ESR for phase sensitive detection measurements and is under control of the instrument's digital signal processor (DSP); the shutter completely blocks light from reaching the detectors in less than 7 ms. The light then enters the spectrometer chamber through the entrance slit ($7 \times 0.3\,\mathrm{mm}^2$) with a calibrated area and slit width and impinges on the Fèry prism. The prism has a concave front surface and a convex aluminized back surface, so only a single

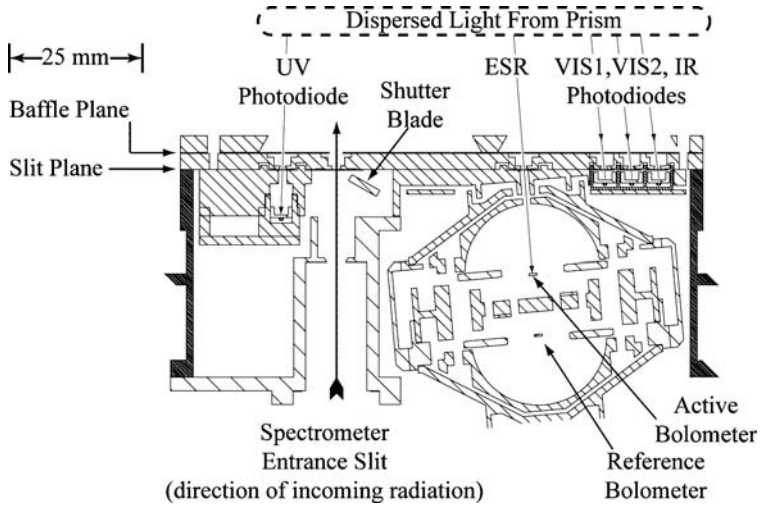

Figure 4. Detail of focal plane assembly to accompany Figure 3. It shows the locations of the five irradiance detectors, the entrance slit and light shutter. The motor to rotate the shutter is below the plane of the diagram, and the CCD (75 mm length) is above the plane.

optical element is needed to disperse and focus the incoming light beam on the focal plane that contains five irradiance detectors, the ESR plus four photodiodes.

For broad wavelength coverage applications a prism spectrometer has a distinct advantage over an equivalent grating spectrometer. The prism produces only a single spectral order whereas the grating would produce overlapping spectral orders that would need to be removed. Likewise, the well-polished prism produces far less scattered light than an equivalent grating. The resolution of the instrument is determined from the spectrometer design geometry and the glass wavelength dispersion (i.e., the first derivative of the index of refraction). The spectrometer's resolving power ($\lambda/\Delta\lambda$) is a strong function of wavelength and varies from 378 at 250 nm, to a minimum of 37 at 1260 nm, and increases slowly in the infrared to 142 at 2700 nm. Section 2.3.2 will describe the optical and spectroscopic properties of this instrument.

2.2.2. *The Wavelength Control Path*

The wavelength control path provides the prism rotation angle which is then combined with other measured instrument parameters to give the wavelength that reaches each of the focal plane detectors (see Section 2.3.3). Very precise wavelength control is needed for radiometric measurements of the solar spectrum; otherwise, small unknown wavelength shifts will translate into signal changes that could be falsely interpreted as solar variability. Sunlight enters the instrument through the CCD entrance slit (3 mm tall $\times$ 0.1 mm wide) after a series of field-of-view limiting baffles and a set of wavelength limiting glass filters. Note that this is a

separate entrance slit from the spectrometer entrance slit discussed in the previous section. The light beam impinges on a spherical mirror (steering mirror) that makes an image of the entrance slit on a 12000 element linear array located in the instrument's focal plane. By having the control knowledge in the focal plane, rather than at the axis of rotation, possible spectral shifts caused by thermal drifts and distortion are minimized. The CCD is read out and peak detection electronics locate the position of the image on the CCD; this information is used in a servo control system that compares the commanded position to the current image position (equivalently, the prism rotation angle) and this information is updated every 25 ms. The full angular rotation of the drive is only $\pm 2.5^\circ$, so a flexure is used in the place of a bearing-based rotator to eliminate bearing noise and backlash. Likewise, a suspended voice coil is used to rotate the flexure since very fine motion control and low actuation noise can be obtained with this device compared to stepper and DC drive motors.

2.2.3. *The Prism Transmission Measurement Path*

Degradation in the optical system is expected, and two independent on-orbit methods are used to measure prism transmission degradation – the single largest source of long-term uncertainty in the irradiance measurement. The first method simultaneously compares the responsivity of the two SIM channels where one channel is exposed to sunlight less that 1/5th of the time of the primary channel. The second method is to define an optical path that uses one spectrometer to deliver monochromatic light to the other so a direct measure of the prism transmission can be obtained. This third optical path (see Figure 2) is symmetric, so SIM A can be used to calibrate Prism B and vice-versa. The two instruments are coupled with a periscope that consists of two concave spherical mirrors mounted at 45° with an intermediate slit located in the wall that separates the two instruments. The periscope is positioned in the instrument so an image of the entrance slit is formed at this intermediate slit with imaging properties nearly identical to the spectrometer's exit slits. The folding mirror mechanism permits the measurement of the light intensity before and after it passes through the prism and the ratio of these two intensities gives the prism transmission. This on-board prism calibration system is designed as a relative transmission measurement for tracking long-term changes. Because the periscope mirrors affect the polarization, the absolute transmission is measured with a ground calibration system that does not use the periscope system. The in-flight transmission measurement details are discussed in Section 2.3.4.

2.2.4. *Instrument Vacuum/Pressure Enclosure*

The only common component in the SIM A and SIM B spectrometers is the vacuum/pressure vessel that has separate vacuum doors for each of the two spectrometers, in case one of the doors failed to open after launch. Designing the instrument housing in this manner has a number of advantages. (1) The instrument is pumped out and degassed to remove volatile organics and water vapor thereby protecting

the optical components from surface contamination. (2) The enclosure is designed to hold a pressure of 1.2 atmospheres. During spacecraft/launch vehicle integration and pre-flight environmental testing the instrument is backfilled with high purity argon to maintain cleanliness. Likewise, the instrument was launched with an Ar backfill. (3) The vacuum doors are equipped with fused silica windows so the optical paths can be stimulated for pre-flight integration and test, and first light check-out after launch. (4) The instrument case can be evacuated to a pressure $\sim 10^{-8}$ atmospheres for laboratory testing of the ESR detectors. (5) After launch and 4 weeks of spacecraft outgassing, the instrument was opened to space vacuum through a bleed valve. After final evacuation the vacuum doors were opened.

2.2.5. *Generic Channel Interface (GCI) Instrument Control*

SIM uses the same GCI unit described by McClintock, Rottman, and Woods (2005) but it is reconfigured for specific SIM activities. The GCI consists of three boards. A digital signal processor (DSP) board, based on the Temic TSC21020F processor, performs the most important tasks for the instrument. It performs the bridge excitation and readout of the ESR (see Section 3.3), multiplexing and readout of the photodiodes, shutter actuation, and prism drive control (see Section 3.2). A multifunction board has H-bridge circuitry to control bi-stable mechanisms, proportional controllers for instrument heater control, and conditioned low-voltage power. An interface board accepts command and control instructions from the flight computer, performs housekeeping monitoring, and packetizes and transmits housekeeping and DSP science data back to the flight computer.

2.3. DETAILS OF THE SIM INSTRUMENT

Section 2.2 gave an overview of the SIM instrument design that meets the requirements to measure solar spectral variability, and this section will provide details on the design and performance of these subsystems.

2.3.1. *ESR and Photodiode Detectors*

The known solar irradiance spectrum, the area and width entrance slit, and the dispersion of the spectrometer can be used to estimate the power collected by the instruments detectors. The greatest power observed will be about 40 μW near 800 nm, and the signal is down about a factor of 470 in the ultraviolet (260 nm) and a factor of 65 at infrared (2700 nm). To make measurements with a precision of 100 ppm the noise equivalent power must be on the order 4 nanowatts. This value sets the design goal for the ESR. In order to keep the thermal mass of the detector small, a $1.5 \times 10\,\mathrm{mm}^2$ bolometer is used in the place of the cone geometry typically used for TSI measurements and the bolometer is surrounded by an optical quality sphere to increase the inherent blackness of the bolometer and to thermally isolate it from its surroundings. Figures 3 and 4 show the ESR location in the instrument case and the focal plane assembly. Thermal detectors have slow response times,

and therefore are not suitable detectors for spectral scanning purposes. Therefore, complementary photodiode detectors are also used to allow a fast scan mode, but the radiant sensitivity of the photodiodes are calibrated against the ESR routinely in-flight.

The primary innovation of the SIM ESR over other radiometers described in Hengstberger's comprehensive book (1989) is the use of phase sensitive detection. There are, in fact, two phase locked loops used in the detection of radiant power. The first is a high-frequency (50 Hz) loop implemented in hardware that controls the excitation of a precision AC resistor/thermistor bridge, and the second is a low-frequency (0.01 Hz) light chopper operating at the minimum of the detector's noise spectrum and the phase sensitive detection is handled in data processing (Lawrence *et al.*, 2000).

The fundamental underlying principle of electrical substitution radiometry is to establish a constant thermal environment on two independent black surfaces (bolometers) using Joule heating from resistors in intimate contact with the surfaces so that the difference in temperature between the surfaces approaches 0. When one of these surfaces (the active bolometer) is exposed to radiant energy, a measurable temperature difference is generated between the active and reference bolometers. Joule heating on the active bolometer must then be reduced until its temperature equals that of the reference bolometer ($\Delta T \simeq 0$). When this condition is met, the electrical power removed equals the radiant power incident on the active surface to within the magnitude of the noise associated with the temperature measurement.

Figure 5 shows the block diagram implementation of the ESR. Very small temperature differences are measured with a Wheatstone Bridge circuit using matched spinel thermistors in two arms of the bridge excited by a 50 Hz cosine wave

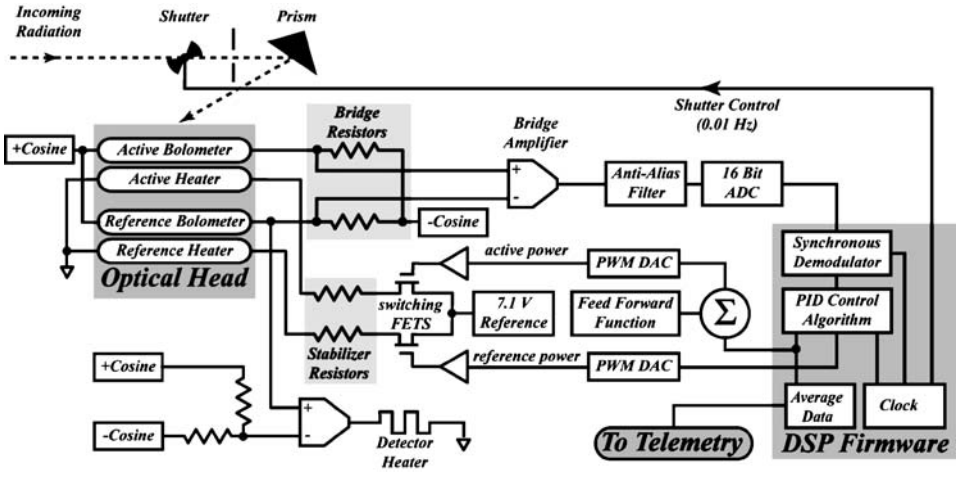

Figure 5. Block diagram of the SIM ESR circuitry. The system employs two phase locked loops: shutter operates at 0.01 Hz, and the thermistor bridge in the optical head is driven by a 50 Hz cosine wave.

generated by the DSP firmware. A precision 7.1 V voltage source (LTZ 1000, Linear Technologies Inc.) in conjunction with the heater resistors produces an equilibrium temperature value of 32 °C on both the active and reference bolometers. Switching MOSFET (Metal Oxide Semi-Conductor, Field Effect Transistor) transistors modulate the power to the heaters with a 50% duty cycle square wave. Electrical substitution on the active bolometer is achieved by pulse width modulating the heater waveform when radiant energy impinges on the detector; in this way the power delivered to the bolometer is proportional to the duty cycle. Control of the active bolometer duty cycle occurs in DSP firmware where the conditioned and digitized bridge temperature error signal is filtered by a PID (proportional/integral/differential) algorithm. The PID algorithm controls the closed-loop response of the servo system. A pulse width modulated digital-to-analog converter (PWM DAC) converts the 16-bit digital output from the loop filter to the power applied to the replacement heater. The output of the loop filter is scaled and clipped to a unipolar code ranging from 0 to M – 1, where $M = 64\,000$. This code counts the width of the pulse on the gate of the MOSFET switch that pulses the voltage source to the heaters. The replacement heaters on the SIM bolometers are not precision resistors and vary by about 100 ppm. Therefore series stabilizer resistors of equal value are included in the circuit. The nominal power per data number for the SIM ESR is:

$$A = V_{\mathrm{ref}}^2 \frac{R_H}{(R_H + R_s)^2} \frac{1}{M} \cong 2 \times 10^{-9} (\mathrm{Watts/DN}) \quad \text{where:} \begin{array}{c} V_{\mathrm{ref}} = 7.1\ V \\ R_H = 100\,k\Omega \\ R_s \approx R_H \\ M = 64\,000 \end{array} . \quad (1)$$

The reference thermistor also provides the signal for a proportional heater (rather than a PWM heater) to maintain a constant temperature environment for the two bolometers. This heater circuit is also controlled by the DSP using a similar PID algorithm to the one used to balance the bridge. As is discussed in greater detail in Harder *et al.* (2005), a feed-forward function is supplied to add a predetermined power step to the control loop. This allows an end-to-end measurement of the servo gain thereby giving a measure of stability and degradation of the ESR electronics.

Figure 6 shows the mechanical/optical/thermal implementation of the SIM ESR with a cross-sectional rendering of the detector showing the location of the active and reference bolometers inside the thermal enclosure (panel a), and two microscope images showing the construction of the detector (panels b and c). In Figure 6, the detector is shown in the spectrometer's cross-dispersion direction (tall dimension of the exit slit) while Figure 4 shows a cross-section in the dispersion direction. The bolometer is a 1.5 × 10 × 0.03 mm CVD (chemically vapor deposited) diamond substrate that detects radiation on the front surface and a replacement power resistor is located on the back surface. The thermal enclosure places the two bolometers in a uniform thermal environment, but optically isolates them so that light entering the

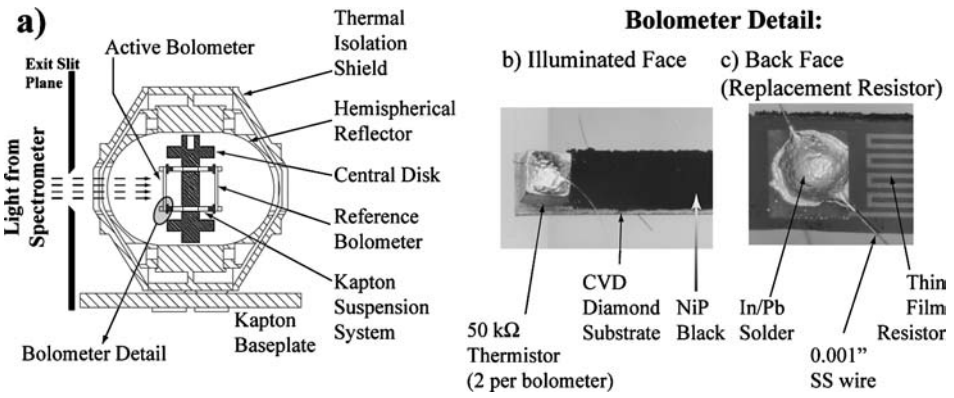

Figure 6. Panel (a) shows a cross-sectional view of the ESR detector and identifies critical components. Panel (b) shows a microscope photograph of the front face of the bolometer with one of the spinel thermistor soldered onto the diamond substrate along with the NiP surface. There are two series thermistors on the front face at opposite ends. Panel (c) shows the back face of the bolometer with the stainless steel wire soldered onto a gold pad. The thin film resistor is evident in this photograph as well.

detector cavity directly illuminates the active bolometer, but cannot propagate to the reference bolometer. The front surface of each bolometer has two 50 k Ω spinel thermistors in series soldered at opposite ends of the strip and a layer of nickel phosphorous black (NiP) is deposited in the center portion of the bolometer for radiation absorption (Johnson, 1980). The back surface of the bolometer has a thin film resistor photo-etched onto the diamond substrate and covers the same area as the NiP black layer on the front side of the detector.

The custom-made photodiodes used for SIM are $10 \times 2\,\text{mm}^2$ for the three silicon photodiodes (International Radiation Devices Inc., Torrence, CA) and $8 \times 2\,\text{mm}^2$ for the InGaAs photodiode (Hamamatsu Corporation, Bridgewater, NJ). The Vis1 and UV silicon photodiodes have *n*-on-*p* construction with a nitride passivated SiO_2 layer to stabilize their radiant sensitivity in the ultraviolet. The Vis2 photodiode is constructed similarly, but with p-on-n geometry. Figure 4 shows the location of these detectors in the instrument's focal plane. The detectors are located 2 mm behind the exit slit for the VIS1, VIS2, and IR photodiodes, but the UV diode is placed 10 mm behind the exit slit to improve the rejection of scattered light. A baffle is placed 2 mm in front of the exit slits to limit the field-of-view of the detectors to the solid angle subtended by the prism. The photo current for each detector is converted to a voltage by a precision transimpedance amplifier, and these voltages are multiplexed and digitized by the same 16-bit bipolar analog-to-digital converter.

2.3.2. *Optical and Spectroscopic Properties*

The nominal properties of the SIM spectrometer and detectors are summarized in Table I. The Fèry prism spectrometer is analogous to the Rowland Circle concave grating spectrometer (Warren, Hackwell, and Gutierrez, 1997). This spectrometer

TABLE I
SIM optical properties.

Parameter	Value				
Spectrometer					
Wavelength coverage	200 –2700 nm				
Focal length	400 mm				
F-number					
Solar	115				
Spectrometer	16 (Dispersion), 22 (Cross dispersion)				
Prism glass	Suprasil 300				
Prism figure					
Front surface radius	421.48 mm				
Back surface radius	441.27 mm				
Central thickness	12.30 mm				
Wedge angle	34.49 mm				
Projected aperture	25 mm				
Prism height	18 mm				
Measured focal length	403.15				
Surface roughness	0.75 Å (RMS)				
Focal plane aberrations	5 μm				
Entrance slit dimensions					
Slit width	0.3 mm				
Slit length	7.0 mm				
Field-of-view					
Dispersion	2.8°				
Cross dispersion direction	1.7°				
Detectors	UV	ESR	Vis1	Vis2	IR
Range (nm)	200 –308	255–2700	310 –1000	360 –1000	994–1655
Material	*n-p* silicon		*n-p* silicon	*p-n* silicon	InGaAs
Detector size (mm)	2 × 10	1.5 × 10	2 × 10	2 × 10	2 × 8
Exit slit width (mm)	0.34	0.30	0.30	0.30	0.30
Nominal location (mm)	−10	35	50	55	60

design is limited to high *f*-number applications because of significant image degradation due to coma and astigmatism that occur even at moderate numerical apertures. However, this is not an issue for the 1/2° solar geometry where the aberrations are only about 5 microns in the focal plane. The radii of curvature for the front and back surfaces of the prism are optimized so that the minimum RMS (root mean

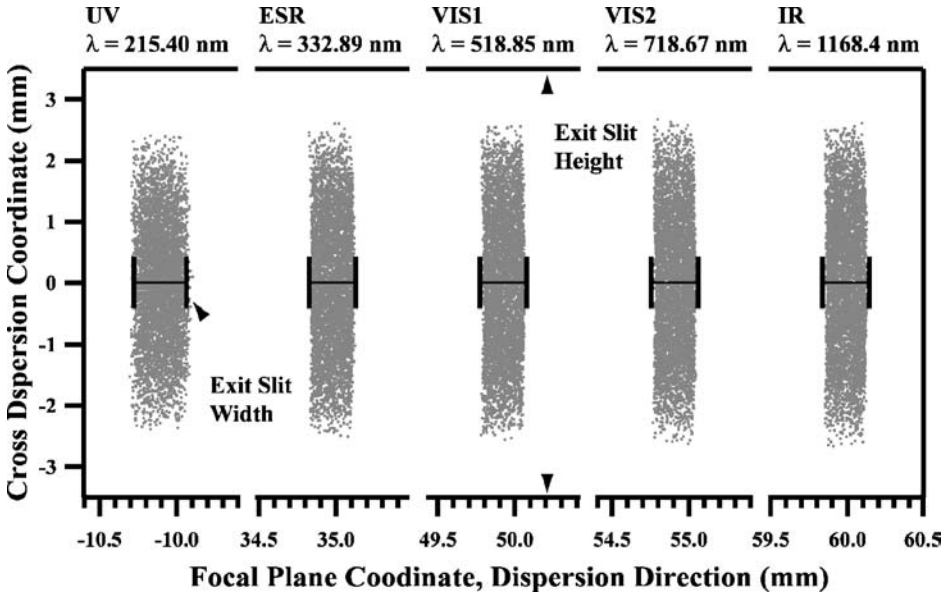

Figure 7. Spot diagrams for the five focal plane detectors at a fixed prism rotation angle of 59.5°. The figure shows the range of the slit width and height in focal plane coordinates and the center wavelength of light that goes through the appropriate exit slit.

square) spot size is attained at the location of the ESR exit slit (ZEMAX, Focus Software Inc., San Diego, CA).

Figure 7 shows a focal plane spot diagram at each detector's exit slit at a fixed prism rotation angle of 59.5° (generated by IRT, Parsec Technology Inc., Boulder, CO). At this prism rotation angle, the prism disperses white light and each detector observes a different wavelength simultaneously. The ray trace analysis assumes the origin is at the center of the entrance slit and uses the actual measured positions of the slits and prism; this figure shows that the UV photodiode detector is on the opposite side of the entrance slit from the other four detectors. This figure shows the effects of coma and spherical aberration on images; they have about 5 μm of curvature due to coma and the images are about 5 mm tall because the instrument focal plane is at the horizontal focus (focus in the dispersion direction) of the tilted spherical mirror back surface of the prism. The vertical focus (focus in the cross dispersion direction) is located behind the entrance slit at a distance of $\sim 2d$ where d is the distance from the face of the prism to the horizontal focus; ~400 mm for SIM. The exact location of the tangential focus is a function of the prism refractive index, therefore, the height and width of the image at the exit slit is wavelength dependent as well. For the ESR, VIS1, VIS2, and IR exit slits the image is demagnified in the dispersion direction, so the instrument function (the convolution of the entrance and exit slit at fixed wavelength) is trapezoidal in form. The image distortion is the worst at the location of the UV photodiode, and the image is magnified so a

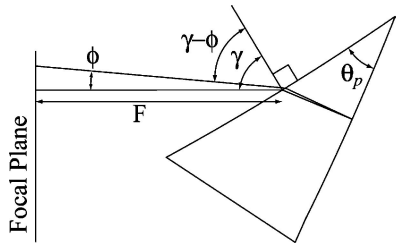

Figure 8. Shows the geometry of the Fèry prism spectrometer that is described in Equation (3).

wider exit slit (340 μm instead of 300 μm) is used to partially compensate for the significantly wider spot width. In all cases the height of the image at the exit slit is smaller than the entrance slit, but the exit slits are made to be 7 mm tall to match the entrance slit and so light is not vignetted with off-axis spacecraft pointing in the cross-dispersion direction. These wavelength dependent aberrations have a small, but significant, effect on the radiometric performance of the instrument. Because the instrument cannot be focused equally well at all wavelengths and all focal plane positions simultaneously, the exits slits are slightly over-filled and the peak of the trapezoidal instrument function does not reach a value of 1.0 for most wavelengths; a value of 1.0 corresponds to the case where all the photons at the entrance slit pass through the exit slit (assuming a perfectly transmissive prism). The worst case is a 1.4% deficit near the instrument's resolution minimum at 1.2 μm for the ESR detector. Ray tracing with measured instrument parameters can accurately model these radiometric deficits that are then included in the final radiance calculation.

The instrument dispersion model is based on prism geometry derived from Snell's law and applies to a prism in Littrow configuration (James and Sternberg, 1969). Figure 8 shows the geometry of the spectrometer: the variables are the prism incidence angle with respect to the first surface normal vector, γ, the deviation angle, ϕ, the index of refraction of fused silica, n, the prism wedge angle, θ_p, and the instrument focal length, F, produced by the prism's spherical surfaces. The index of refraction of fused silica is given from the three-term (six coefficient) Sellmeier Equation measured by Malitson (1965) at 20 °C and is valid to 10 ppm:

$$n_{20}(\lambda) = \sqrt{1 + \sum_{j=1}^{3} \frac{\lambda^2 K_j}{\lambda^2 - L_j^2}} \quad \begin{array}{ll} \mathrm{K_j} & \mathrm{L_j} \\ 0.6961663 & 0.0684043 \\ 0.4079426 & 0.1162414 \\ 0.8974794 & 9.896161 \end{array} . \tag{2}$$

This paper also gives the temperature dependence of the index of refraction; the data from Figure 3 of his paper was digitized and fit to 1 ppm with a 5th order polynomial as a function of wavenumber in inverse microns and is incorporated in SIM data processing. The $\mathrm{d}n(\lambda)/\mathrm{d}T$ dependence is significant so $n(T)$ is calculated at each prism rotation step with prism temperatures recorded in instrument telemetry.

The basic relation between the angles shown in Figure 8 and the index of refraction is given by

$$2\theta_p = \sin^{-1}\left[\frac{\sin(\gamma)}{n}\right] + \sin^{-1}\left[\frac{\sin(\gamma - \phi)}{n}\right]. \quad (3)$$

In general, this equation can be rearranged to give each of the variables as a function of the others and then related to other instrument subsystem parameters and the validity of this equation can be checked against ray tracing. This topic is discussed in detail in Harder *et al.* (2005).

The irradiance detectors are located at focal plane positions to maximize their wavelength coverage and remain within the $\pm 2.5^\circ$ rotation range of the prism drive mechanism; see Figure 4 for the relative locations of the detectors in the focal plane. Because the detectors are at different locations in the focal plane, the prism rotation angle reported by the CCD position encoder system has a different wavelength value at each detector position. Figure 9 shows the mapping of wavelength into prism rotation angle for each of the focal plane detectors; the extent of the curves for each detector also reflects the ranges over which the data are valid. This figure shows the position and wavelength coverage of the periscope that was described in Section 2.2.2. Like the other focal plane detectors, the extent of the curve indicates the valid operating range for the prism calibration system. The curvature seen in these traces is caused by the non-linearity of fused silica's dispersion ($dn/d\lambda$). When a vertical line is drawn through Figure 9 at a fixed prism angle, the intersection of the detector curves with this line indicates the wavelengths that each detector simultaneously observes; if this vertical line does not intersect one of the detector traces then that detector will not respond at that rotation angle. Likewise, a horizontal cut of constant wavelength indicates the needed prism rotation angle for a requested wavelength at each detector, and if this horizontal line intersects two or more detector curves, then

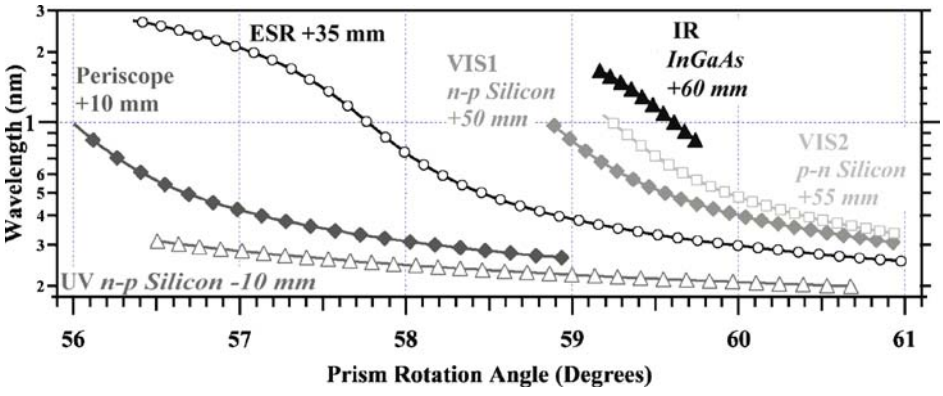

Figure 9. Wavelength is plotted as a function of prism rotation angle for each of the five focal plane detectors and the periscope that couples the two instruments together for prism transmission measurements. This figure also gives the valid operating wavelength ranges for each detector.

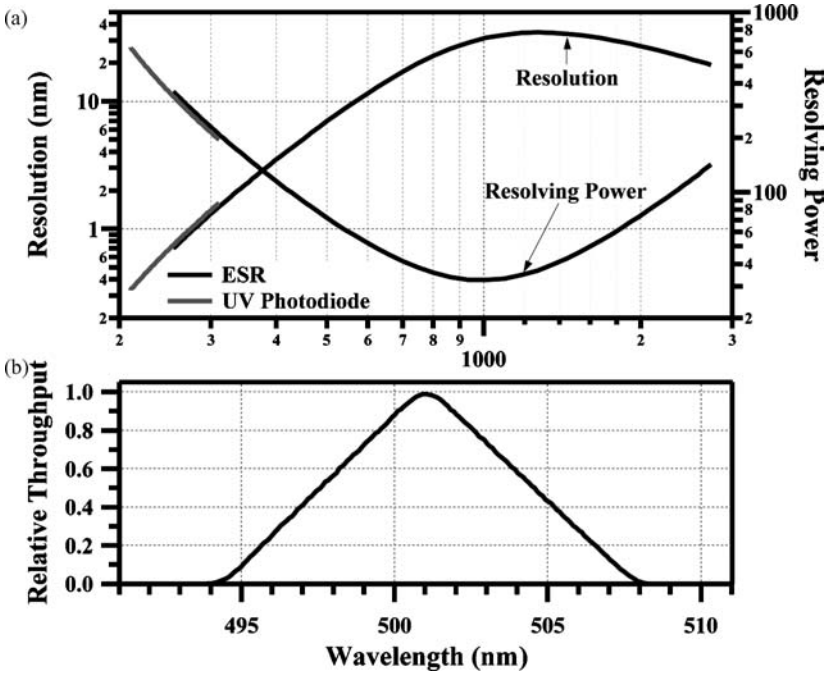

Figure 10. Panel (a) shows the FWHM resolution and the resolving power ($\lambda/\Delta\lambda$) of the SIM instrument for two detectors, ESR, and UV. The resolution function is slightly different at each detector position in the instrument focal plane, so the two traces do not overlap. Panel (b) shows the instrument function at 501.02 nm with a half-width of 7.06 nm. The throughput of the instrument at the peak is 0.996 because of image overfilling of the exit slit.

there is wavelength overlap between these detectors. This is particularly important since the ESR is used to calibrate the photodiode detectors and this indicates the range over which the calibration will be effective for each detector.

The spectral resolution and resolving power ($\lambda/\Delta\lambda$) of the instrument are given in Figure 10a for the ESR and the UV photodiode detector to show the full wavelength range. Refraction geometry produces a slightly different resolution function for each detector, but data processing accounts for these differences. The resolution, as defined here, is given by the full-width-half-maximum (FWHM) of the asymmetric trapezoidal instrument function. The asymmetry is caused by non-uniform $dn/d\lambda$ over the span of a slit width along with spectrometer aberrations. The resolving power is greatest in the ultraviolet, decreases to a minimum near the minimum deviation angle of the prism, and slowly increases again in the infrared.

Figure 10b shows a particular instrument function profile for a peak value of 501.02 nm, a FWHM profile width of 7.06 nm, and the peak throughput is 0.996 instead of 1.0 because of slit overfilling. Ray tracing the spectrometer with the known instrument geometric parameters and the fused silica refractive index generates this instrument function. Because the instrument profile changes smoothly

with wavelength, a set of profiles is ray traced on a uniform index of refraction grid and their trapezoidal properties are parameterized (rising and falling slopes and intercepts, and value at the peak). Interpolating these parameters generates an instrument function for an arbitrary wavelength. In practice the FWHM of the resolution function is not used in the calculation of spectral irradiance, but rather the integral of the profile; this topic will be discussed in detail in a companion paper (Harder *et al.*, 2005).

For the SIM instrument, six spectral samples per slit width are used as a compromise between the need for high sampling and the length of time available on an orbit to complete all the needed activities. The instrument function shown in Figure 10b is shown as a function of wavelength, but when plotted as a function of focal plane coordinate, y, instead of wavelength the instrument functions are nearly identical in shape regardless of wavelength. The integrals of relative throughput as a function of y differ by only 300 ppm from 250 to 2500 nm. This implies that spectral scans of constant y step size produce equivalent sampling of the resolution function regardless of the wavelength, and a change in the spectral sampling is not needed as the prism dispersion changes. High spectral sampling is needed because the solar spectrum at the SIM resolution typically varies by 4% over an exit slit width, so high spectral sampling is necessary to follow the light curve over the course of a scan. Because of the temperature dependence of the index of refraction, the wavelengths reported by the instrument are not consistent from scan to scan, so spectra must be interpolated onto a uniform wavelength grid for spectral comparisons. The high spectral sampling used here is needed to maintain radiometric accuracy during this interpolation process.

2.3.3. *Prism Drive Operation and Block Diagram*

The wavelength control path discussed in Section 2.2.2 achieves very high precision by using a linear 12000 element CCD to measure the prism rotation angle in the focal plane rather than at the point of rotation as is done by most angular rotation encoders. The CCD, prism turntable, and the voice coil actuator form an electro-mechanical closed-loop system to control the incident angle of the prism (the variable γ in Figure 8).

Figure 11a shows an electro-mechanical block diagram for the closed-loop operation of the prism drive. The principle of operation is based on the comparison of two counters: one counter measures in near real-time the center location of the light spot on the CCD by measuring the length of time needed to reach that position at a constant video sweep rate, and the other counter measures the length of time needed to reach a predetermined target position on the CCD; the time difference between these two counters gives the servo error. A single 2.5 MHz clock inputs the position down counter and sets the CCD video readout rate after it is divided by 5; this effectively subdivides a CCD pixel by a factor of 5 and increases the spatial resolution of the measurement. The SIM DSP asynchronously loads the target position into the position down counter terminal count register, and a synchronizing

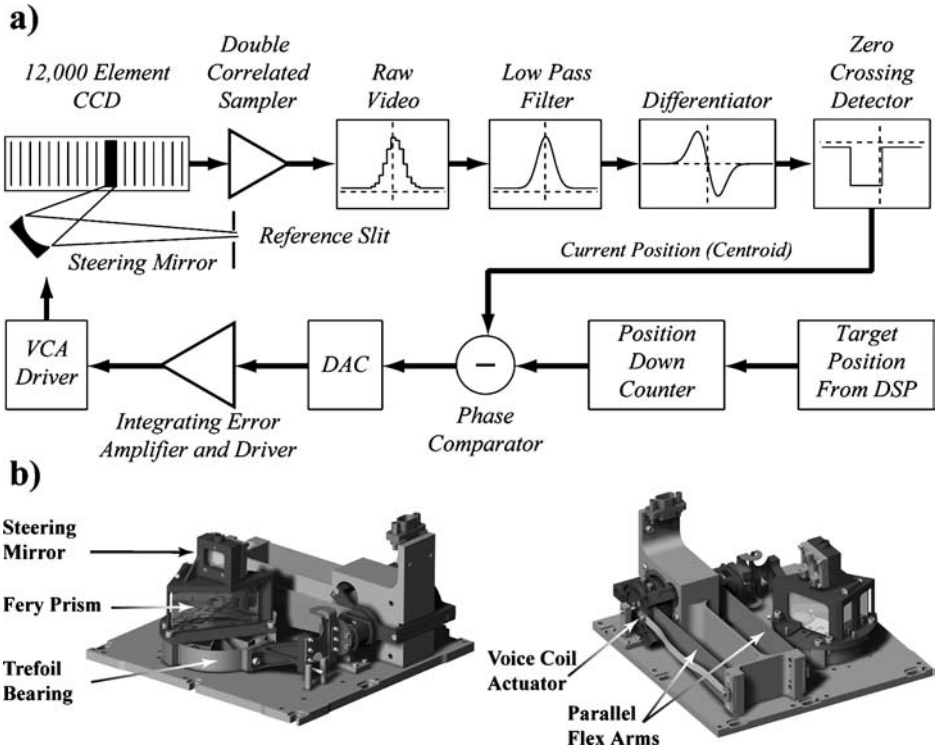

Figure 11. Panel (a) Electro-mechanical block diagram of the SIM prism drive system. The diagram shows the process of comparing a down counter with the video sweep of the CCD. Panel (b) is two views of the prism drive identifying important attributes to the mechanical design of the drive.

pulse enables the down counter and initiates the sweep of the CCD. The location of the image spot on the CCD is detected and conditioned by double correlated sampler electronics, low-pass filtered, differentiated, and this smoothed waveform is fed into a zero crossing detector so the length of time needed to reach zero crossing can be obtained. The phase comparator determines the difference in time, whether positive or negative, and creates a pulse that is fed to the bi-polar digital-to-analog converter (DAC) and then an integrating power amplifier drives the voice coil actuator (VCA) that rotates the prism/steering mirror to move the light spot on the CCD. The location of the image spot relative to the target position is updated every 25 ms. The time constant of the integrating amplifier determines the slew rate of the mirror.

For the prism drive electronics to work the rotation mechanism must provide very smooth and low noise motion. This prism drive is shown in Figure 11b. Drive power is furnished through a linear voice coil actuator suspended by parallel flex arms with ∼6 mm of motion (BEI Sensors and Systems Inc., model LA13-12-000A). The voice coil is coupled to a radial flexure, a custom trefoil bearing, which supports the prism and steering mirror. The most important attribute of this flexure-based system

TABLE II
Prism drive attributes.

Parameter	Value
Position repeatability	1.3 μm or 0.65 arcsec
Drive jitter	0.3 μm or 0.16 arcsec
Position update rate	Every 0.025 s (40 Hz)
Step response for 50 μm step	0.3 s

is that it is almost noise-free since there are no rolling or sliding bearings. The absence of backlash helps the stability of the servo system, and the elastic properties of the flexure materials permit the very fine pointing needed for drive reproducibility. This system is mechanically stiff in the rotation plane, but is soft in the out-of-plane direction so the trefoil bearing and the voice coil actuator sub-assemblies must be individually constrained to prevent torques generated under launch vibration conditions from damaging the drive. Extensive vibration testing was performed to ensure its survivability during launch and that it could not 'jam' under vibration conditions. The prism was bonded to an invar plate and then mounted onto the trefoil bearing. Invar was used to match the temperature expansion coefficient of fused silica so the bonding material does not experience shear forces when instrument temperatures change in space. Table II lists the performance specification achieved for the drive.

2.3.4. *In-Flight Prism Degradation Measurements*
Two in-flight calibration operation modes track long-term degradation of the instrument. The first is a direct prism transmission calibration that uses the calibration path introduced in Section 2.2.2 and depicted in Figure 2, and the second is a direct SIM A/SIM B spectrometer comparison. Prism transmission is a first order term in the SIM radiometric measurement equation (Harder *et al.*, 2000a; Harder *et al.*, 2005), and changes from the ground-based prism transmission measurement must be tracked throughout the mission. This radiation effect is significant for SIM, but the rate and wavelength dependence of in-flight prism transmission degradation is well-characterized and presented in detail by Harder *et al.* (2005). The mechanism for the observed prism degradation is not well known, but is most likely due to hard radiation and/or energetic particle modification of the fused silica surface of the prism itself or a thin film ($< 5 \times 10^{-10}$ m) of organic material contaminating that surface. The findings of Havey, Mustico, and Vallimont (1992) from the LDEF Experiment (Long Duration Exposure Facility) are suggestive of the effects observed in SIM but do not give evidence of the degradation mechanism.

The transmission of the SIM prisms was measured in the laboratory on ground witness prisms manufactured from the same bole of Suprasil 300 as the flight units that were polished and coated simultaneously (Harder *et al.*, 2005). Ray trace analysis shows that light rays propagate almost normal to the mirrored surface of the

prism so the mirror reflectivity is nearly independent of prism incident angle (see Figure 8). The transmission of the prism can be decomposed into three contributions: (1) Fresnel surface losses (both vacuum-to-glass and glass-to-vacuum), (2) light attenuation in the bulk of the glass, and (3) reflective losses on the aluminized back surface. Therefore, the transmission can then be calculated for each detector by combining the reflective/bulk losses with the Fresnel reflection loss to give the total transmission.

For the in-flight transmission re-calibration, only the relative time dependence of the transmission as a function of wavelength is needed so corrections for systematic light losses are not accounted for by the in-flight method described here. To obtain a true transmission measurement (as was done for the laboratory method), it is necessary to account for non-symmetric light losses in the I and I_o measurement paths, polarization effects, and the spatial dependence of radiant sensitivity of the detector.

A cross-sectional view of the periscope is shown in Figure 12a depicting the chief ray propagation of light through the periscope. It couples the two instruments and

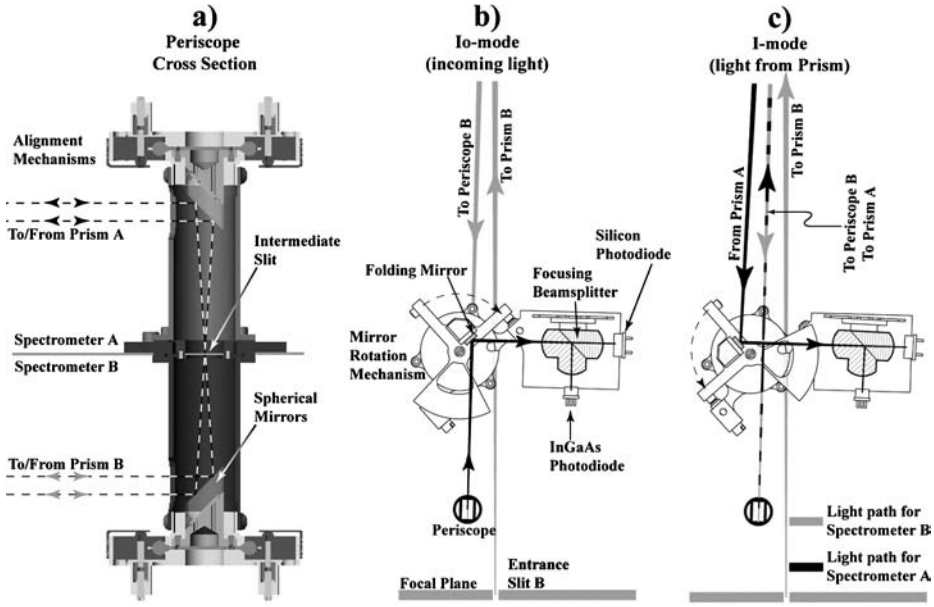

Figure 12. Panel (a) shows a cross-sectional view of the periscope and the propagation of light through it. Panels (b) and (c) show the opto-mechanical system to perform the prism transmission calibration. In this figure SIM B is calibrating the prism transmission of SIM A. The visual perspective is looking down on spectrometer A with its rays colored black. SIM B (mirror-image of SIM A) is directly underneath SIM A and hidden in this view, but the light rays of SIM B are colored in gray and projected onto the page to show their optical path. Monochromatic light is selected by SIM B and directed through the periscope to spectrometer A. Panels (b) and (c) show the light paths to give the I_o and I modes along with the orientation of the mirror rotation mechanism, respectively.

consists of two 45° spherical mirrors (1038 mm radius) separated by an intermediate slit that matches the spectrometer's entrance and exit slits (0.3×7 mm); the spherical mirrors are on-center and concave. There are two optical requirements for the periscope: (1) the periscope images prism A onto prism B (and visa-versa), and (2) the periscope images the entrance slit onto the intermediate slit just as if it were another focal plane exit slit. Figure 9 includes the wavelength range and prism rotation angle used for the calibration system.

The prism transmission relies on a mirror rotation mechanism that moves a flat mirror into one of two fixed locations. Its action is shown in Figures 12b and 12c. The design and location of the calibrator mechanism in the instrument case is set to ensure that in the event of the rotation mechanism failure no light paths to the focal detectors can be vignetted. The focusing beamsplitter is designed to have a 10 mm focal length to keep it compact, and images the folding mirror onto the two detectors. This optical element has to be able to image the diverging beam from the periscope onto essentially the same area of the detector as the converging beam returned from the prism. The beamsplitter coating is a non-polarizing broadband coating that has a flat ~35% transmission/reflection throughout the 300 to 1000 nm region.

To perform a prism transmission calibration at one wavelength, the following sequence of commands is executed. Assume that the transmission of prism A is to be measured.

1. Referring to Figure 12b, the entrance shutter to spectrometer A is closed and the shutter to spectrometer B is opened. Sunlight through entrance slit B is dispersed by prism B and a selected wavelength λ_{cal} passes through the periscope intermediate slit. Light is directed by a flat mirror mounted on the bi-stable rotation mechanism to the focusing beam splitter that feeds two detectors for the UV/visible and IR wavelength bands. The intensity of light measured by these detectors gives the I_o term, or the intensity of light before its passage through the prism.
2. Referring to Figure 12c, the turntable mechanism then rotates the mirror by 88.4° and is now out of the beam but still aligned with the optical axis of the calibration detectors. The prism A is rotated to a pre-selected angle so that light can pass through the prism and travels back to the flat mirror where it is then detected a second time to give the term I. Ratio of I to I_o gives the prism transmission factor at λ_{cal}.

Because spectrometer channels A and B are identical and mirror-image each other, the prism B transmission can be calibrated by an analogous procedure. The hard radiation trap is located in the optical train to minimize unnecessary exposure during the measurement. This procedure is repeated at 44 different wavelengths in the 300 to 1000 nm region on a weekly basis, and the data are used in the SIM exposure model described by Harder *et al.* (2005).

The second in-flight calibration mode for this instrument is to compare the two spectrometers. Spectrometer B is exposed to ionizing radiation on a much lower duty cycle so its optics will not degrade at the same rate as SIM A, which is used for daily measurements. The two spectrometers are operated simultaneously in the absolute irradiance mode so the instrument comparison excludes possible spacecraft pointing, solar, and thermal differences that would affect the comparison if the measurements were conducted in a serial fashion. The spectral irradiance for the A and B channels are calculated independently using the prism transmission procedure for each channel independently. The resultant irradiance measurements from spectrometers A and B can then be used to validate the prism transmission measurement and to identify other sources of degradation in SIM.

2.4. Flight instrument operation modes

A number of instrument operation, housekeeping, and calibration modes have been developed for SIM to maintain measurement accuracy, account for the limited wavelength ranges of the detectors, and monitor changes in instrument responsivity. These operation modes are tabulated in Table III along with a description of the action and the frequency that these operation modes are executed. In this table, cadence is the number of events that occur within a specified number of days. The operating modes for SIM A and SIM B are identical except that SIM B is directly exposed about 18% of the time of SIM A. When either channel of SIM is operated, the HRT is usually in the optical train to reduce prism exposure.

The ESR is an inherently slow detector so the photodiodes are used to track the orbit-to-orbit variability of the Sun and the ESR is used to calibrate the radiant sensitivity of the diodes. During a nominal 58-min sunlit portion of an orbit, the typical plan is to perform a 24-min photodiode scan along with part of an ESR table sequence. This is repeated over nine orbits until all 63-table positions are completed, and the process is then repeated. The table wavelength positions are selected to occur at maxima and minima in the solar spectrum so the irradiance measurement is less sensitive to possible wavelength shifts over the span of a measurement. Both the ESR table and the photodiode scans are performed with the HRT both in and out of the light beam. In this way solar variability can be followed without excessive and unnecessary exposure to the prism. During the course of the day, only three orbits have the HRT out of the beam; two for 24-min scans, and one for the ESR infrared scan. The ESR infrared scan is used to acquire daily spectra at wavelengths longer than the 1.7 μm cutoff of the InGaAs photodiode. The ESR is used in a phase sensitive mode with the shutter operating at 0.05 Hz and two shutter cycles per prism step. The spectrum is measured with two samples per slit width, not quite meeting the Nyquist criteria, but permitting the spectrum to be acquired in a single orbit. The ESR full scan provides the best measurement of the solar spectrum, but requires 240 sunlit minutes to complete, so solar variability likely occurs during

TABLE III
SIM irradiance and calibration modes.

Mode name	Cadence (number/days)	Action
Irradiance measurement modes		
24-min photodiode scan	9-13/1	Measure solar irradiance with the 4 photodiodes over their full operation range; 6 samples/slit width sampling; includes measurement of photodiode dark signal; 2 scans/day are without HRT.
ESR table sequence	12/7 HRT in 1/7 HRT out	63 selected wavelengths; 0.01 Hz shutter frequency; 2 shutter cycles per wavelength step.
ESR infrared scan	1/1	Spectral scan with ESR as primary detector in the 1200 –2700 nm range; 2 samples per slit width; 0.05 Hz shutter frequency; 2 shutter cycles per prism step.
ESR full scan	1/90	Complete scan of solar spectrum with ESR as primary detector; 0.05 Hz shutter frequency; 2 shutter cycles per prism step; 3 samples/slit width; 15 orbits to complete scan.
Calibration/housekeeping modes		
Fixed wavelength	1/1	Study thermal stability of instrument and detector noise. Performed with shutter frequency of 0.05 Hz.
Prism transmission	1/7	44 discrete wavelengths; see Section 2.3.4 for action; measure the transmission of both prisms.
ESR gain	2/7	Measure closed loop gain on ESR at 0.05 and 0.01 Hz.
Cruciform scan	1/7	Check alignment of instrument to spacecraft. Prism rotation angle held at a fixed wavelength by open-loop prism drive control; cycles through 6 different positions.
CCD image dump	1/7	Read out CCD video to track intensity of image spot and evaluate progress of CCD radiation damage.

(*Continued on next page*)

TABLE III
(*Continued*)

Mode name	Cadence (number/days)	Action
A/B comparison	1/30	Perform both photodiode scans and table sequence without HRT on both instruments simultaneously.
Field-of-view (FOV) map	1/180	Measure solar spectra on a 5×5 spatial grid with a 0.125° spacing. Spacecraft offset pointing is used to generate the map. Measures the spatial extent of radiation damage on the prisms; performed with HRT in the beam.

this time frame. Therefore, the ESR full scan is done in conjunction with a 24-min scan and spread over 15 orbits to complete. In this way, the comparison of the ESR full scan with multiple photodiode scans determine the degree of solar variability over the course of the day.

The weekly calibration/housekeeping modes are spread uniformly to eliminate gaps in the coverage of solar variability. The prism transmission calibration is performed at 39 wavelengths and requires 300 s to complete an individual wavelength, so six orbits are occupied to complete the experiment for SIM A and B.

The cruciform scan and the FOV map are spectrometer operations performed in conjunction with planned spacecraft offset pointing maneuvers. The SORCE spacecraft has excellent pointing accuracy of better than 1 arcmin, pointing knowledge of 10 arcsec, and jitter of 5 arcsec/s, so instrument pointing corrections are not normally required. However, effects of prism degradation have a gradient across the 3×11 mm light spot on the face of the prism so monitoring the changes in transmission across this illuminated spot is important. For the cruciform scans, the spacecraft slews across the instrument's field-of-view in the dispersion and cross dispersion directions at a rate of 1.5 arcmin/s for a range of $\pm 4^\circ$. With pointing offsets this large, the steering mirror that illuminates the CCD will lose signal to the point where it cannot control, so open-loop fixed wavelength positioning is used for this mode of operation. These cruciform scans supply information about the relative alignment of the instrument with respect to the spacecraft attitude control reference. They supply information about the spatial extent of transmission degradation on the face of the prism, and they also give information about scattered light in the instrument. The FOV maps are a 5×5 mm, 7.5 arcsec mapping of the prism response and are performed with closed-loop control. The full wavelength range of the instrument is measured at each of these 25 positions over the span of about 4 days with frequent measurements of the reference center position to remove

bias from solar variability. The FOV maps provide the best information about the degradation gradient on the face of the prism.

3. Conclusions

This paper describes the SORCE SIM instrument. It is a prism spectrometer operating over the spectral range of 200 to 2700 nm. It employs an electrical substitution radiometer as the primary detector, a CCD as an absolute encoder of prism rotation angle measured in the focal plane of the detectors, and is capable of providing self-calibration of prism degradation by using one spectrometer to deliver monochromatic radiation to the other. The instrument uses phase sensitive detection to determine the irradiance, but also employs low noise photodiodes to acquire the spectrum in a rapid scan mode.

Acknowledgements

The authors gratefully acknowledge the entire staff at LASP, both students and professionals, who contributed to the success of this new instrument throughout concept, design, fabrication, integration, test, and launch phases of the program, as well as the current data processing staff. This research was supported by NASA contract NAS5-97045.

References

Anderson, G. P. *et al.*: 1999, *SPIE Proc.* **3866**, 2.
Curcio, J. A. and Petty, C.: 1951, *J. Opt. Soc. Am.* **41**, 302.
Harder, J. W., Lawrence, G. M., Rottman, G., and Woods, T. N.: 2000a, *Metrologia* **37**, 415.
Harder, J. W., Lawrence, G., Rottman, G., and Woods, T.: 2000b, *SPIE Proc.* **4135**, 204.
Harder, J. W., Fontenla, J., Lawrence, G., Woods, T., and Rottman, G.: 2005, *Solar Phys.*, this volume.
Havey, K., Mustico, A., and Vallimont, J.: 1992, *SPIE Proc.* **1761**, 2.
Hengstberger, F.: 1989, *Absolute Radiometry*, Academic Press Inc., San Diego, California.
Hood, L. L.: 1999, *J. Atmos. Sol. Terr. Phys.* **61**, 45.
James, J. F. and Sternberg, R. S.: 1969, *The Design of Optical Spectrometers*, Chapman and Hall LTD, London, p. 41.
Johnson, C. E.: 1980, *Metal Finishing*, 21.
Kiehl, J. T. and Trenberth, K.: 1997, *Bull. Am. Met. Soc.* **78**, 197.
Kopp, G., Lawrence, G. M., and Rottman, G.: 2003, *SPIE Proc.* 5171.
Kurucz, R. L.: 1991, in A. N. Cox, W. C. Livingston, and M. S. Matthews (eds.), *Solar Interior and Atmosphere*, University of Arizona Press, Tucson, Arizona.
Labitzske, K. and Van Loon, H.: 1988, *J. Atmos. Sol. Terr. Phys.* **50**, 197.
Lawrence, G. M., Rottman, G., Harder, J., and Wood, T.: 2000, *Metrologia* **37**, 415.
Lean, J. L.: 1991, *Rev. Geophys.* **29**, 505.

London, J., Rottman, G., Woods, T., and Wu, F.: 1993, *Geophys. Res. Lett.* **20**, 1315.
McClintock, W., Rottman, G., and Woods, T.: 2005, *Solar Phys.*, this volume.
Malitson, I. H.: 1965, *J. Opt. Soc. Am.* **55**, 1205.
Neckel, H. and Labs, D.: 1984, *Solar Phys.* **90**, 205.
Reid, G. C.: 1991, *J. Geophys. Res.* **96**, 2835.
Reid, G. C.: 1999, *J. Atmos. Sol Terr. Phys.* **61**, 3.
Rottman, G. J., Woods, T., and Sparn, T.: 1993, *J. Geophys. Res.* **98**, 10667.
Rottman, G., Harder, J., Fontenla, J., Woods, T., White, O., and Lawrence, G.: 2005, *Solar Phys.*, this volume.
Smith, R. C. and Baker, K.: 1978, *Limnol. Oceangr.* **23**, 260.
Solanki, S. K. and Unruh, Y.: 1998, *Astron. Astrophys.* **329**, 747.
Thuillier, G., Hersé, M., Labs, D., Foujols, T., Peetermans, W., Gillotay, D., Simon, P., and Mandel, H.: 2003, *Solar Phys.* **214**, 1.
Vanhoosier, M. E., Bartoe, J.-D. F., Brueckner, G. E., Prinz, D. K., and Cook, J. W.: 1981, *Solar Phys.* **74**, 521.
Viereck, R. and Puga, L.: 1999, *J. Geophys. Res.* **104**, 9995.
Warren, D. A., Hackwell, J., and Gutierrez, D.: 1997, *Opt. Eng.* 3**6**, 1174.
White, W. R., Lean, J., Cayan, D., and Dettinger, M.: 1997, *J. Geophys. Res.* **102**, 3255.
Willson, R. C.: 1988, *Space Sci. Rev.* **38**, 203.